University of Reading

Deep self-organizing map neural networks improve the segmentation for inadequate plantar pressure imaging data set

Article

Accepted Version

Wang, D., Li, Z., Dey, N., Slowik, A., Sherratt, R. S. ORCID: https://orcid.org/0000-0001-7899-4445 and Shi, F. (2025) Deep self-organizing map neural networks improve the segmentation for inadequate plantar pressure imaging data set. Network: Computation in Neural Systems, 36 (2). pp. 322-342. ISSN 1361-6536 doi: 10.1080/0954898X.2024.2413849 Available at https://centaur.reading.ac.uk/119027/

It is advisable to refer to the publisher's version if you intend to cite from the work. See Guidance on citing.

To link to this article DOI: http://dx.doi.org/10.1080/0954898X.2024.2413849

Publisher: Taylor and Francis

All outputs in CentAUR are protected by Intellectual Property Rights law, including copyright law. Copyright and IPR is retained by the creators or other copyright holders. Terms and conditions for use of this material are defined in the End User Agreement.

www.reading.ac.uk/centaur

University of Reading

CentAUR

Central Archive at the University of Reading

Reading's research outputs online

Deep Self-Organizing Map Neural Networks Improves the Segmentation for Inadequate Plantar Pressure Imaging Data Set

Dan Wang[1], Zairan Li[1, *], Nilanjan Dey[2], Adam Slowik[3], R. Simon Sherratt[4], and Fuqian Shi[5]

1. Wenzhou Polytechnic, Wenzhou, 325067 China
2. Department of Computer Science and Engineering, Techno International New Town, Kolkata, 700156 India
3. Department of Electronics and Computer Science, Koszalin University of Technology, Koszalin, Poland
4. Department of Biomedical Engineering, the University of Reading, Reading, UK
5. Rutgers Cancer Institute of New Jersey, New Brunswick, 08903 NJ, USA

*Corresponding author: Zairan Li, Address: Wenzhou Polytechnic, 1 University Rd., Ouhai, Wenzhou, 325035. Email: lzr198206@126.com, Tel: +86-57786680118, Fax: +86-577-86680090

Abstract: This study introduces a deep self-organizing map neural network based on level-set (LS-SOM) for the customization of a shoe-last defined from plantar pressure imaging data. To alleviate the over-segmentation problem of images, which refers to segmenting images into more subcomponents, a domain-based segmentation model of plantar pressure images was constructed. The domain growth algorithm was subsequently modified by optimizing its parameters. A SOM with 10, 15, 20, and 30 hidden layers was compared and validated according to domain growth characteristics by using merging and splitting algorithms. Furthermore, we incorporated a level set segmentation method into the plantar pressure image algorithm to enhance its efficiency. Compared to the literature, this proposed method has significantly improved pixel accuracy, average cross-combination ratio, frequency-weighted cross-combination ratio, and boundary F1 index comparison. Using the proposed methods, shoe lasts can be designed optimally, and wearing comfort is enhanced, particularly for people with high blood pressure.

Keywords: Deep neural network, level set, region growth plantar pressure imaging, self-organizing map, shoe-last optimal design.

1 Introduction

There are several problems with the analysis and exploitation of plantar pressure imaging data, including a single processing method, incomplete information acquisition, and a weak model for processing the data, even though plantar pressure imaging analysis methods are only being studied to design optimal shoe lasts. By using imagery generated from plantar pressure data, the work presented in this paper aims to improve the extraction method for key regions related to the formation of comfortable shoes. In the field, the critical issue is to develop a segmentation model that is more accurate using intelligent information processing. To optimize the shoe's last design, segmentation efficiency evaluation is used to obtain accurate area division, extract the features required for the optimal design, and provide data services. Over the past decade, technology has developed rapidly for detecting and analyzing pressure gait on plantar with improved measurement indicators. Besides sports, clinical medicine and rehabilitation medicine also use it widely. Acupuncture and targeted rehabilitation training programs were studied. Scholars introduced a method for detecting and evaluating lower extremity injuries based on the characteristics of plantar pressure distribution (Pereira et al. 2021 and Gao et al. 2016). By using the image features of pressure-sensitive imaging to achieve the segmentation of key areas, the design of the bottom surface of a comfortable shoe last can be optimized based on key point data of plantar pressure. Pressure-sensitive imaging poses the challenge of selecting an efficient segmentation method based on its inherent characteristics. Preprocessing, feature definition, selection of plantar pressure imaging, parameter adjustment, and optimization of learning algorithms are involved. Following is the organization of the remaining chapters. In chapter II, we present the relevant literature. In chapter III the modeling of a level-set-based self-organizing mapping neural network, including domain growth segmentation, and how it is combined with the SOM network. Chapter IV includes the experiment design, acquisition and processing of data, and a comparison of results. Finally, conclusions are provided in chapter V.

2 Literature Review

It is important to build a solid link between image processing and image content understanding through image segmentation. Image segmentation methods based on threshold theory, pixel area, pixel edge, and a specific theory, among others, are the main approaches. With the development of artificial intelligence technology, image segmentation technology has gradually occupied a very important position in many methods of image dimensionality

reduction (Li et al. 2021). Aguiar et al. (Aguiar et al. 2019) improved the segmentation algorithm of a class of images using cross-entropy combined with meta learning methods and achieved good results. Image segmentation combined with some current specific theories and methods has made significant progress, such as the level set variational model (LBF) proposed (Liu et al.2019). In addition, the combination of artificial neural network (ANN), convolutional neural network (CNN), and multi-feature combination methods, Laplacian operator and Canny operator are also very useful in the study of image segmentation. It is generally believed that general image segmentation models and algorithms can be applied to plantar pressure images. In terms of feature selection, the texture of an image is currently considered to be a common and applicable feature (Patel et al. 2023 and DiMattina 2022).
Due to their capabilities in distributed information storage, parallel processing, and self-learning, ANNs have also been widely used in pattern recognition, smart control, and system modeling. Wu (Wu et al. 2018) used CNN to combine residual learning and densely connected network to make more full use of the features of each layer and shorten the path between low-level feature maps to high-level feature maps by adding short connections, thereby efficient segmentation of retinal blood vessel images is achieved.
This study proposes a high-efficiency semantic segmentation model for images. Image segmentation algorithms based on deep learning outperform traditional image segmentation algorithms in terms of performance and effectiveness (Chouhan et al. 2018). Wang (Wang et al. 2019) explains how to select a neural network model, how to set key training parameters, and how to imp=rove its effectiveness; no specific deep learning technique has been developed for plantar pressure imaging. Also, it is challenging to label the functional area of plantar pressure, identify the clusters of plantar area, and segment the functional area pressure image accurately. Based on the image domain, deep learning algorithms for segmentation include RefineNet, PSPNet, and ResNet. Visual geometry group, a deep learning algorithm for engineering algorithms has also been included (Kemker et al. 2018, Hofbauer et al. 2019 and Zhang et al. 2019). VGG-Net is a platform for developing deep convolutional neural networks. In VGG-Net, the relationship between neural network depth and performance is investigated. A 16-19-layer deep CNN can be constructed with VGGNet by repeatedly stacking small convolution kernels of 3x3 and max-pooling layers of 2x2. VGG-Net has a lower error rate than the previous State-of-the-Art network structure. VGG-Net employs all 3x3 small convolution kernels and all 2x2 maximum pooling kernels (Dhomne et al. 2018 and Chavan et al. 2018). To overcome the time-consuming and computational complexity of ANNs. Babu et al. (Babu et al. 2021) predicted Parkinson's disease (PD) using metacognitive radial basis function networks (McRBFNs). Erkaymaz et al. (Erkaymaz et al. 2012) presented SW-FFANN, a classification feedback ANN model. In addition, the application of pulse coupled neural networks in image classification is also a very important reference for this topic.

Kohonen's Self-Organizing Maps (SOM) (Kohonen 2021) simulated the brain's signal processing by using an unsupervised learning method that emulates clustering and high-dimensional visualization. the initialization of the competition layer of the SOM will also have an impact on the results (Ali et al. 2019 and Kamal et al. 2017). SOM learning mimics the function of the human neural network. Self-organizing machine learning can solve problems in almost all IT fields, so a gigantic artificial intelligence system with functions beyond people's imagination can be built through infinite self-organizing machine learning (Chang et al. 2014).

We introduce a novel deep self-organizing map neural network, LS-SOM, specifically designed for customizing shoe lasts using plantar pressure imaging data. To mitigate over-segmentation, we propose a domain-based segmentation model tailored to plantar pressure images. The novelty of the research is,

(1) leverages advanced techniques to address the over-segmentation problem inherent in plantar pressure images, thereby improving the accuracy and efficiency of segmentation.
(2) In addition to the LS-SOM, we incorporate a level-set segmentation method into the plantar pressure image algorithm to further enhance segmentation efficiency. This integration improves the accuracy and reliability of the segmentation process, contributing to more precise shoe last designs.
(3) conduct a thorough evaluation of the LS-SOM by comparing models with different numbers of hidden layers (10, 15, 20, and 30). Through rigorous validation based on domain growth characteristics using merging and splitting algorithms, we identify the optimal architecture for shoe last customization.

3 Modelling

In this section, our domain-based segmentation model, level-set improved, and deep self-organizing map neural network is introduced.

3.1 Domain-based Segmentation Model

3.1.1 Domain Value Selection and Region Segmentation

Let a pixel point be (x, y), its value is $f(x, y)$, and T is a given threshold, then we defined a threshold function g as follow,:

$$g(x)=\begin{cases}255 & f(x,y)\geq T\\ 0 & f(x,y)<T\end{cases} \tag{1}$$

Where, $g(x)$ is the binary image after threshold operation; the selection of T is difficult and the deviation is large. The following is an example of an iterative threshold selection method:

Step 1: Given an initial threshold value T .

Step 2: Segment image into two regions of T , R_A is the first region, and R_B is the second region.

Step 3: Calculate average gray of all pixels in regions of R_A and R_B , and denoted as μ_A and μ_B .

Step 4: update the threshold by $T^k=(\mu_A+\mu_B)/2$, $k=1,2,\ldots$

Step 5: increased $k=k+1$

Step 6: go to **Step 2** until $T^k<T$.

Let z denote the gray value, and $P(z)$ denote the estimated value of the probability density function of the gray value. Probability density functions represent the gray values of one background, while the second represents the gray value of the foreground (that is, the object in the image), and the hybrid density function describes the overall grayscale transformation in the image is defined as,

$$P(z)=P_1(z)+P_2(z) \tag{2}$$

Where, P_1 and P_2 are the probability of occurrence of a pixel with value z in the foreground and background, respectively, and $P_1+P_2=1$. For a given threshold T , the probability of front and background misclassification is,

$$E_1(T)=\int_{-\infty}^{r}\left(1-P_1(z)\right)dz \tag{3}$$

Similarly, we have that,

$$E_2(T)=\int_{-\infty}^{r}\left(1-P_2(z)\right)dz \tag{4}$$

Then the total error rate is,

$$E(T)=P_1E_1(T)+P_2E_2(T) \tag{5}$$

Where E_1 , and E_2 are errors on T. If the normal distribution is theoretically satisfied, that is, the Gaussian distribution, we can define $P(z)$ as,

$$P_i(z)=\frac{1}{\sqrt{2\pi}\sigma_i}e^{-\frac{(z-\mu_i)}{2\sigma_i}}\ (i=1,2) \tag{6}$$

Where, μ is the mean, σ is standard deviation. e is Euler's number. When $\sigma^2=\sigma_i^2$, then, we have that,

$$T=\frac{\mu_1+\mu_2}{2}+\frac{\sigma^2}{\mu_1-\mu_2}\ln\left(\frac{P_2}{P_1}\right) \tag{7}$$

If $P_2=P_1$, then T can be simplified by,

$$T=\frac{\mu_1+\mu_2}{2} \tag{8}$$

Varying gray levels are a representation of this difference. In this algorithm, the principle of least squares' method of decision analysis is applied. Let the pixel with grayscale i in the image be n_i ; L is the pixel depth and most often 256; the grayscale range is $[0,L-1]$, then total number of pixels is $N=H\times W$, where H is the hight o of the image, W is the width of the image ; each gray level probability is $P_i=n_i/N$, and subject to $\sum_{i=1}^{L-1}P_i=1$. By using threshold T , the grayscale of image can be segmented into regions of $[0,T-1]$ and $[T-1,L-1]$, denoted as C_0 and C_1 separately, then the probabilities are $P(C_0)=\sum_{i=0}^{T-1}P_i$ and $P(C_1)=\sum_{i=T-1}^{L-1}P_i$. Average grayscales are

$\mu_0 = \mu(T)/P_0$ and $\mu_1 = \mu(T)/P_1$, then maximum between-class variance in two regions is given by,

$$\sigma^2 = P_0 P_1 (\mu_0 - \mu_1)^2 \tag{9}$$

Therefore, let T take values in sequence in the range of $[0, L-1]$, the T value with the largest σ^2 is the best region segmentation threshold. This method can not only be used for the selection of a single threshold containing two regions, but also for the selection and calculation of multiple thresholds in multiple regions.

3.1.2 Region Growth Algorithm

To identify the boundary between regions, graph-cutting techniques primarily use discontinuities in grayscale or color attributes. The region growth algorithm plays a vital role in the domain-based segmentation model; Patel RK introduced a maximal stable extremal region method using machine learning (Patel et al. 2023). Segmentation and merging of regions involve dividing an image into uniform regions. The entire image will be our starting point. As a result, splitting the image becomes straightforward. Determine which areas require processing, i.e., non-uniform areas. The homogeneous regions are placed in the regions list instead of the processing list when they are removed from it. Growing a region (merging) from one pixel is the only way to grow (merge). Region-growing algorithms are based on image pixels, which can be divided into four and eight connections, respectively. Here we adopted four connections (areas). The algorithm is described as follows:

Step 1: For any region C_i, if $P(C_i) = 0$, then split each area into four connected quadrant areas.

Step 2: Combine any two regions of j, k, $P(C_i \cup C_j) = 1$.

Step 3: Stop the operation when aggregation or splitting is not possible.

3.2 Lebel-set based Segmentation

Osher and Sethian first proposed the level set method in 1988. Let Ω be the bounded open set in R^2; u_0 is the image mapping $\Omega \to R$; $C(s)$ is curve mapping from $[0,1] \to R^2$; ω is open set in Ω, C is the edge denoted by $\partial\omega$. Image u_0 is consisted of two regions, values of all pixels in region 1 are u_0^i, and u_0^0 for region 2. The contour of region 1 can be found from (Kimmel 2024):

$$F(C) = \int_{inside(C)} |u_0(x,y) - c_1|^2 \, dxdy + \int_{outside(C)} |u_0(x,y) - c_2|^2 \, dxdy \tag{10}$$

Where, c_1 and c_2 are average value of inner and outer pixels of curve C individually; it can be seen that the curve C that minimizes the energy function value is the contour of the desired region 1, and the energy value is 0. $inside(C)$ is the inside area of curve C and $outside(C)$ is the outside area of curve C. This model is the energy function above, plus regular terms such as the length of the curve and the area of the area within the curve, as:

$$F(C) = \mu Len(C) + vArea(cinside(C)) + \lambda_1 \int_{inside(C)} |u_0(x,y) - c_1|^2 \, dxdy + \lambda_2 \int_{outside(C)} |u_0(x,y) - c_2|^2 \, dxdy \tag{11}$$

Where, $\mu \geq 0$, $v \geq 0$, λ_1, $\lambda_2 > 0$. $Len(\cdot)$ is the length of the curve. Although formally this function can be written as $F(c_1, c_2, C)$, But since c_1 and c_2 are also functions of C, they can be written directly as $F(C)$, as presented by Li and Li (Li et al 2018). Mumford-Shah functions are used to segment images based on optimality criteria. A piecewise smooth function is used to model the image. During the function, the model distance from the input image, the model's smoothness within the subregion, and the subregion boundary length are penalized. The best segmentation can then be calculated by minimizing the function. Curves are represented by level-set functions. For how to solve the minimum value problem of the Mumford-Shah function, the energy function of the curve C above can be written as the energy function of the level set function ϕ, and then the level set function can be solved. To replace the curve C in Eqn. (11) with ϕ, two functions, abbreviated as H function and δ function, need to be introduced as:

$$H(z) = \begin{cases} 1 & z \geq 0 \\ 0 & z < 0 \end{cases} \tag{12}$$

Derivation on H, we have that,

$$\delta_0(z) = \frac{d}{dz} H(z) \tag{13}$$

Rewriting Eqn. (11) as:

$$F(c_1, c_2, \phi) = \mu \int_{\Omega} \delta(\phi(x,y)) |\nabla \phi(x,y)| \, dxdy + v \int_{\Omega} H(\phi(x,y)) dxdy + \lambda_1 \int_{\Omega} |u_0(x,y) - c_1|^2 \, H(\phi(x,y)) dxdy + \lambda_2 \int_{\Omega} |u_0(x,y) - c_2|^2 \left(1 - H(\phi(x,y))\right) dxdy \tag{14}$$

Where, c_1 and c_2 are:

$$c_1(\phi) = \text{average}(u_0 \mid u_0 \in \{\phi \geq 0\}) \tag{15}$$

$$c_2(\phi) = \text{average}(u_0 \mid u_0 \in \{\phi < 0\}) \tag{16}$$

And continuously, we have that,

$$\frac{\partial \phi}{\partial t} = \delta_{\varepsilon} \left[\mu \cdot \text{div}\left(\frac{\nabla \phi}{|\nabla \phi|} \right) - v - \lambda_1 (u_0 - c_1)^2 + \lambda_2 (u_0 - c_2)^2 \right] = 0 \tag{17}$$

Where, $\phi(0, x, y) = \phi_0(x, y)$ *in* Ω, $\frac{\delta_{\varepsilon}(\phi) \cdot \partial \varphi}{|\nabla \phi| \, \partial \vec{n}} = 0$ *on* $\partial\Omega$, $\vec{n}$ is outer normal of edge $\partial\Omega$, δ function's subscript changed from 0 to ε. Re-defined H and δ in the Euler-Lagrange formula, we have that,

$$H_{\varepsilon} = \frac{\left(1 + \frac{2}{\pi} \arctan\left(\frac{z}{\varepsilon}\right)\right)}{2} \tag{18}$$

$$\delta_{\varepsilon} = H_{\varepsilon}^{'} = \frac{\varepsilon}{\pi} \frac{1}{z^2 + \varepsilon^2} \tag{19}$$

While $\varepsilon \to 0$, respectively converge to H and δ_0, δ_0 basically everywhere 0, and the Euler-Lagrange equation above cannot be solved. And now the support set of δ_{ε} is the entire real number set R, so no matter what the shape of the initial curve is, the global optimal solution can be obtained; in addition, the inner contour can be detected. Here, an iterative method can be used to solve the above partial differential equation. First, the partial differential equation is discretized. Then, the iterative form of the level set function ϕ can be obtained by,

$$\frac{\phi_{ij}^{n+1} - \phi_{ij}^{n}}{\Delta t} = \delta_h(\phi_{ij}^{n}) [\mu \cdot \text{curvature}_{ij} - v - \lambda_1 (u_{0ij} - c_1)^2 + \lambda_2 (u_{0ij} - c_2)^2] \tag{20}$$

The algorithm consists of five steps as follows,

Step 1: Random initialization $\phi^0 = \phi_0$, $n = 0$

Step 2: Calculate c_1 and c_2 by formula (15) and (16);

Step 3: Solve according to iterative formula (20) ϕ^{n+1};

Step 4: Reinitialize ϕ;

Step 5: Check if convergence, if yes, STOP; otherwise, go back to **Step 2**

3.3 Self-Organized Map Networks

3.3.1 Basic Modelling

There are two layers in the SOM. The input layer neurons can receive external information from the output layer neurons through weight vectors. Matching degree is calculated by the input layer. A layer's input data dimension depends on the number of neurons. K is the number of neurons in the output layer. Those neurons with a high matching degree (short distance) are determined to win, while those with a low matching degree (greater distance) are discarded. Weight vectors of winning neurons and neurons in their neighborhood are updated to be closer to pattern vectors. Learning map-ping of the SOM neural network involves two components: selecting the best-matching neurons and updating the weight vector. SOM neural networks are described (Aly et al. 2020).

Step 1: Find the number of clustering categories, that is, the dimension of the category vector, with a constant greater than zero as the error threshold.

Step 2: Specify the input model as,

$$\bar{X} = \{x_1, x_2, \cdots, x_n\} \tag{21}$$

Step 3: Determine the distance between each vector of output neuron weights and the input pattern vector,

$$d_j = \sum_{i=1}^{n} \left(x_i^k - w_{ij}\right)^2 \tag{22}$$

Where, $i = 1, 2, \cdots, n$, $j = 1, 2, \cdots, m$

Step 4: Select the neuron with the smallest distance,

$$d_{j_\min} = \min_{j=1,2,\cdots,n} \{d_j\} \tag{23}$$

Step 5: Update the neighborhood neuron weight vector of the winning neuron by,

$$\Delta w_{ij} = \eta(t)\left(x_i^k - w_{ij}\right) \tag{24}$$

Where, $N_j \in NE_{j_\min}(t), i = 1, 2, \cdots, n$

Step 6: Ensure that the neighborhood size and learning rate of the winner are updated. Then go to **Step 2**.

3.3.2 Level-set based Deep SOM Neural Networks

Unsupervised C-V Modelling

The energy function E(C) of the C-V model can be expressed as:

$$E(C) = \mu \cdot \text{len}(C) + v \cdot \text{area}\left(in(C)\right) + \lambda_1 \int_{\text{For}(C)} \left(I(x) - C_1\right)^2 dx + \lambda_2 \int_{\text{Bag}(C)} \left(I(x) - C_2\right)^2 dx \tag{25}$$

Where, C is the foreground target contour. $I(x) \in R$ is the gray value at the pixel x point. $\mu > 0$ is the smoothness of the regular parameter control curve. $v > 0$ is another foreground area with a large penalty for the regular parameter; $For(C)$ and $\text{Bag}(C)$ represent the foreground and background regions, respectively, and their mean values are C_1 and C_2 respectively, and the control parameters of their energy terms are λ_1 and λ_2, respectively. If the variational level set form is used in Eqn. (25) becomes:

$$\frac{\partial \phi}{\partial t} = \delta_\varepsilon(\phi)\left[\mu k - v - \lambda_1 (I - C_1)^2 + \lambda_2 (I - C_2)^2\right] \tag{26}$$

Where, φ is the level-set function; $\delta_\varepsilon(\phi)$ is the Dirac function; k is the curvature of the curve. We have that,

$$\delta_\varepsilon(\phi) = \frac{1}{\pi} \frac{\varepsilon}{\varepsilon^2 + \phi^2} \tag{27}$$

The parameter ε can control the effective width of $\delta_\varepsilon(\phi)$. The initial value φ^0 of the level set is:

$$\varphi^0 = \begin{cases} \alpha, & \text{foreground} \\ -\alpha, & \text{background} \end{cases} \tag{28}$$

Parameter α satisfies $\alpha \approx 2\varepsilon$. If Ω is the entire image area, the curve C can be expressed as $C = \{x \in \Omega : \phi(x) = 0\}$, then we have the foreground and background $\text{For}(C) = \{x \in \Omega : \phi(x) > 0\}$ and $\text{Bag}(C) = \{x \in \Omega : \phi(x) < 0\}$.

Kernel Self-organizing Mapping with Supervised C-V Modelling

The SOM can represent the topological map structure of the input pattern, that is, the spatial position coordinates of the network neurons are used to represent the intrinsic statistical features contained in the input pattern. Since the self-organizing map has two limitations, the lack of estimation accuracy and the lack of optimal objective function, a kernel-based self-organizing map (KSOM) can improve the topology map structure. Consider a grid P consisting of l neurons characterized by the corresponding set of kernels: $k(x, \varpi_i, \sigma_i)$ and the objective function is defined on the output of the i -th neuron:

$$y_i = k(x, \varpi_i, \sigma_i), \quad i = 1, 2, \cdots, l \tag{29}$$

Then, the winner neuron is defined by,

$$i(x) = \arg\max_i y_i(x),\ j \in P \tag{30}$$

Same as SOM, the neighborhood function $h_{i,j}(x)$ is the monotonically decreasing function of the grid distance from the winner neuron $i(x)$, and r_a is the neighborhood function $h_{i,j}(x)$ range:

$$h_{i,j}(x) = e^{-\frac{\|x_j - \varpi j\|^2}{2r_a^2}} \tag{31}$$

The input of scalar image is one-dimensional pixel gray space, and the output is the weight vector of neurons. After inputting the foreground prior image, the value ϖ_{For} of the foreground image neuron can be obtained after training. After inputting the background prior image, the value ϖ_{Bag} of the background image neuron can be obtained. The use of this prior enables automatic segmentation of foreground objects by guiding the curve in the level set section. The test image will get a foreground contour C at each iteration, and the mapping value of each pixel x in the foreground is the winning neuron in ϖ_{For}.

$$\varpi_{For}(x,C) = \left\{ \varpi_{For,j} \left| \arg\min_j \left\| \varpi_{For,j} - \frac{\int_{For(C)} g_\sigma(x-y) I(y)\,dy}{\int_{For(C)} g_\sigma(x-y)\,dy} \right\| \right. \right\} \tag{32}$$

$$\varpi_{Bag}(x,C) = \left\{ \varpi_{Bag,j} \left| \arg\min_j \left\| \varpi_{Bag,j} - \frac{\int_{Bag(C)} g_\sigma(x-y) I(y)\,dy}{\int_{Bag(C)} g_\sigma(x-y)\,dy} \right\| \right. \right\} \tag{33}$$

And combined with level-set, we have that,

$$\frac{\partial \phi}{\partial t} = \delta_\varepsilon(\phi)\left[\mu k - v - \lambda_1 e_{For} + \lambda_2 e_{Bag}\right] \tag{34}$$

Where, $eI(x) - \varpi_{\text{For}}(x,C)_{\text{For}}(x,C) = (x,C)^2$ and $e_{\text{Bag}}(x,C) = \left(I(x) - \varpi_{Bag}(x,C)\right)^2$.

4 Results and Discussion

4.1 Data Acquisition

A test subject can be managed by the Foot-scan software of the RS-scan plantar pressure data acquisition system. In addition to measuring plantar division, pressure, or pressure, the system can also assess diabetic foot ulcer risk. Indicators include load change rate, plantar length, and width, the direct contact area of the sole, lateral angle of the foot, midline axis of the foot, time trajectory, stability analysis, etc. Customized correction plans are available, as well as batch data export and specific format output functions. In addition to a general version, there are versions for specific application areas as well (Li et al 2019). Fig. 1 shows the scan process in 3D mode.

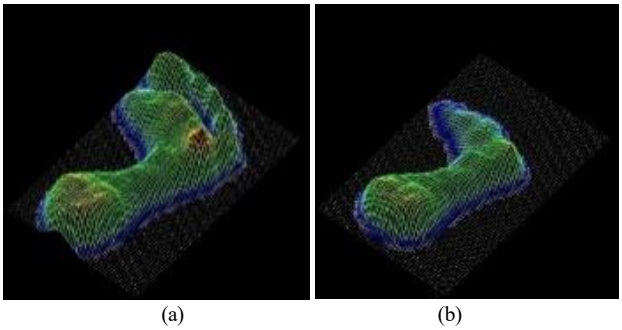

(a) (b)

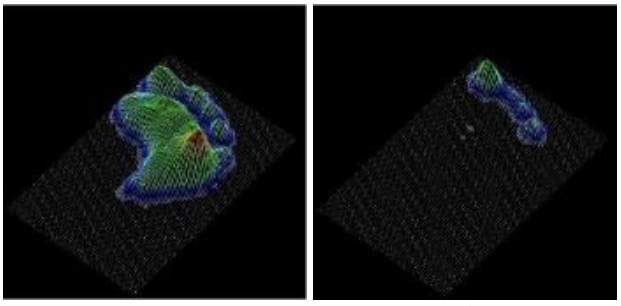

(c) (d)

Fig. 1. Dynamic process of plantar pressure; (a) Maximum contact state, (b) The state when the front foot is raised, (c) Heel lift state, and (d) Front toe contact state.

4.2 Results

Several plantar pressure images were selected from many data sets to illustrate the segmentation effect as can be seen in Fig. 2. Data from a few image sets were selected to simplify the calculation. The first step is to use the segNet platform to process the image (Al-masni et al. 2018). The original image sets are all left foot experiments and are shaped into pulse images in jpg format. Import the split label as shown in Fig. 3 (HL-Heel Lateral, HM-Heel Medial, MF-Mid Foot, Mx-Metatarsal x, and T1-Hallux). Some operating states are shown in TABLE I. Among them, the minimum batch method is a relatively common method, which refers to training only a part of the data set at a time, rather than the entire training set. This can make hardware devices that occupy a small memory footprint and cannot train the entire data set at the same time. The model can be trained. To show the efficiency of the algorithm, a comparative study is carried out. At the same time, using the level set and the seed region growing method to perform segmentation experiments, as shown in Fig. 4 and Fig. 5. Fig. 6 is the optimized result using the level set. A comparison is made with the neural net for traditional pattern recognition illustrated in Fig. 7. The results are shown in Fig. 8. The results for 10, 15, 20, 30 layers SOM are presented in Fig. 9 and Fig. 10. As a result, we increase the number of inputs to 21 with SOM combing with hidden layers of 30 layers and 2000 samples for training. Fig. 11 shows the network structure, and Fig. 12 shows the performance matrix. This network performs best at 24/100 of epochs when the cross-entropy value is lowest. In addition, the ROC curve and fusion matrix evaluated the effectiveness of the proposed network, which has a 99.3% accuracy of classification.

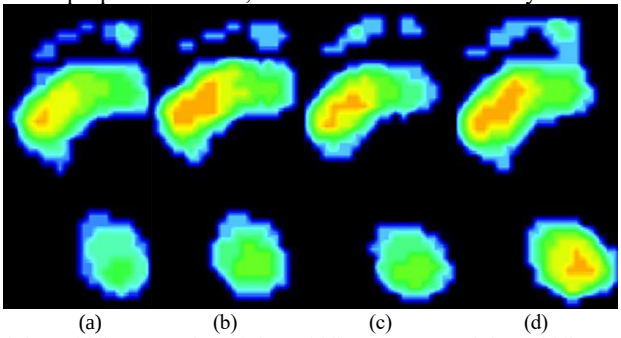

(a) (b) (c) (d)

Fig.2. Original image set; (a) Left foot middle state 1, (b) Left foot middle state 2, (c) Left foot middle state 3, (d) Left foot middle state 4.

TABLE I Platform Parameters for SegNet Training

Iteration	Processing time	Multi-batch accuracy	Mini-batch loss	Learning rate
1	00:00:23	25.23%	0.6544	0.0010
10	00:01:15	32.12%	0.7845	0.0010
15	00:01:35	38.17%	0.8081	0.0010
20	00:01:24	49.24%	0.8159	0.0010

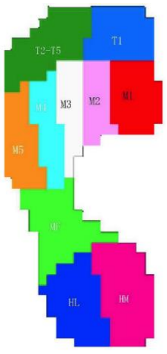

Fig. 3. Plantar pressure imaging segmentation label

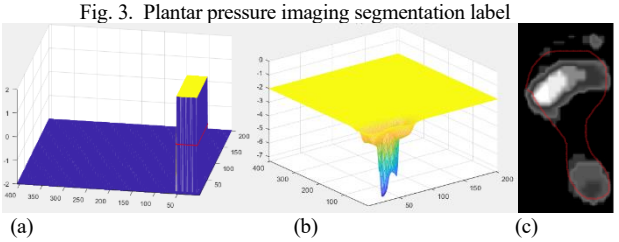

(a) (b) (c)

Fig. 4. Level set segmentation and effect; (a) Function for initializing levels (b) after 200 iterations (c) the segmenting on plantar imaging.

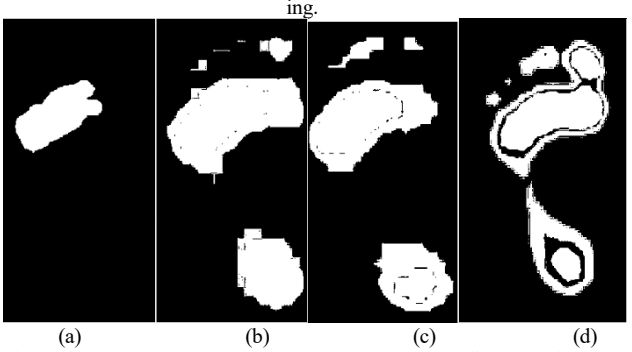

(a) (b) (c) (d)

Fig. 5. Stepwise optimized single-seed region growing segmentation method; (a) initializing levels (b) after 40 iterations (c) after 120 iterations (d) after 200 iterations

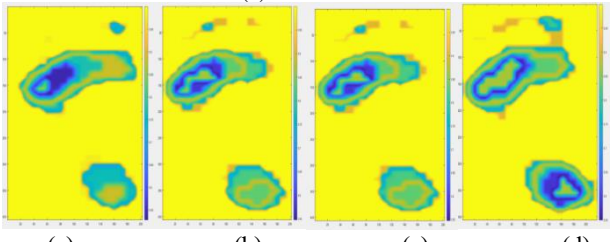

(a) (b) (c) (d)

Fig. 6. Region growing based Level-Set; (a) initializing levels (b) Training state after 40 iterations (c) Training state after 100 iterations (d) Optimized segmentation result.

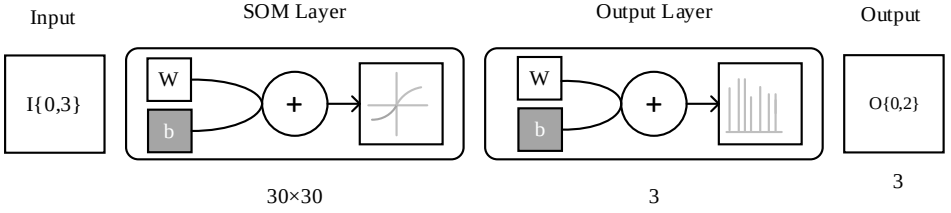

Fig. 7. The structure of SOM network with classification output network.

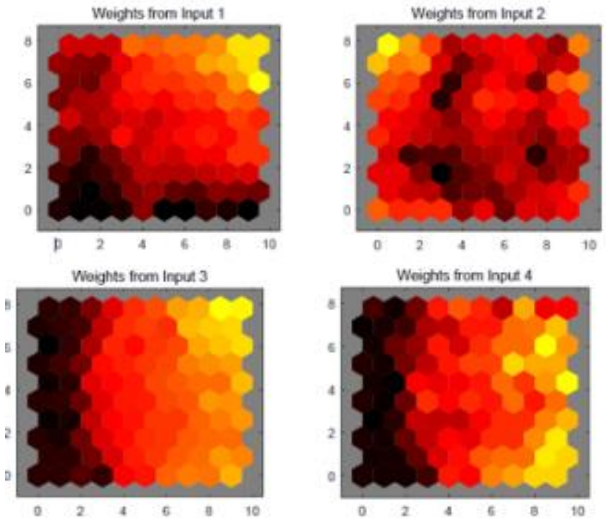

(a)

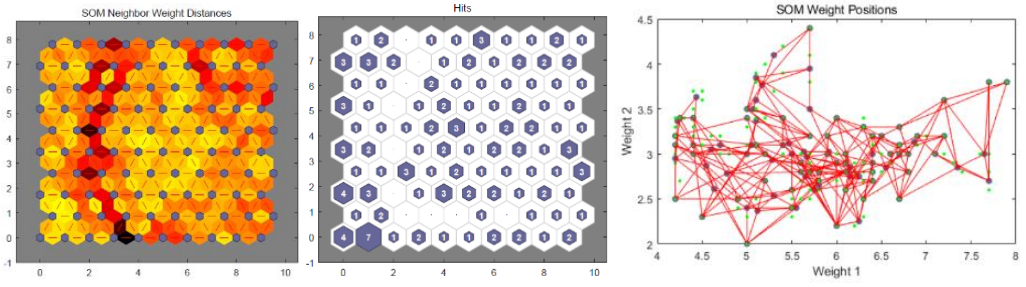

(b) (c)

Fig. 8. SOM training results; (a) Input weights, (b) Distance between SOM neighbors and the hits display, (c) Positions of SOM weights.

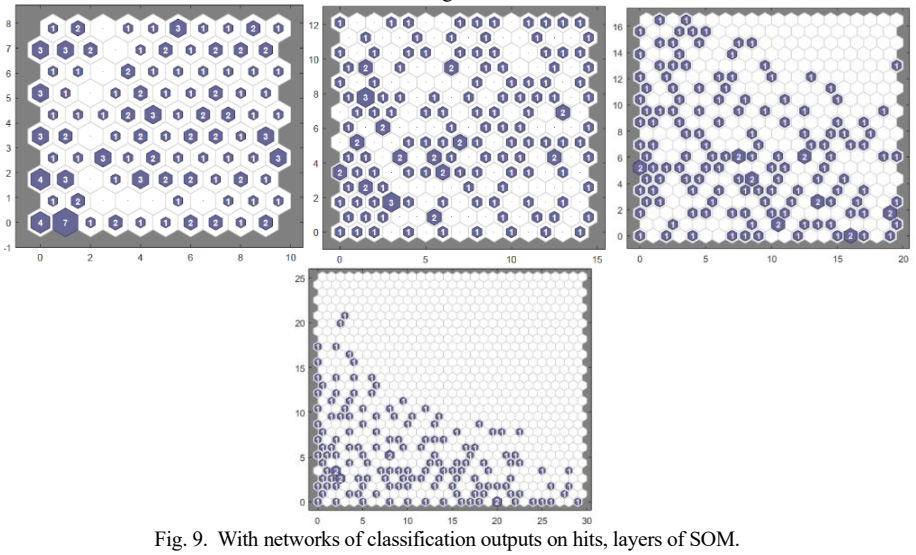

Fig. 9. With networks of classification outputs on hits, layers of SOM.

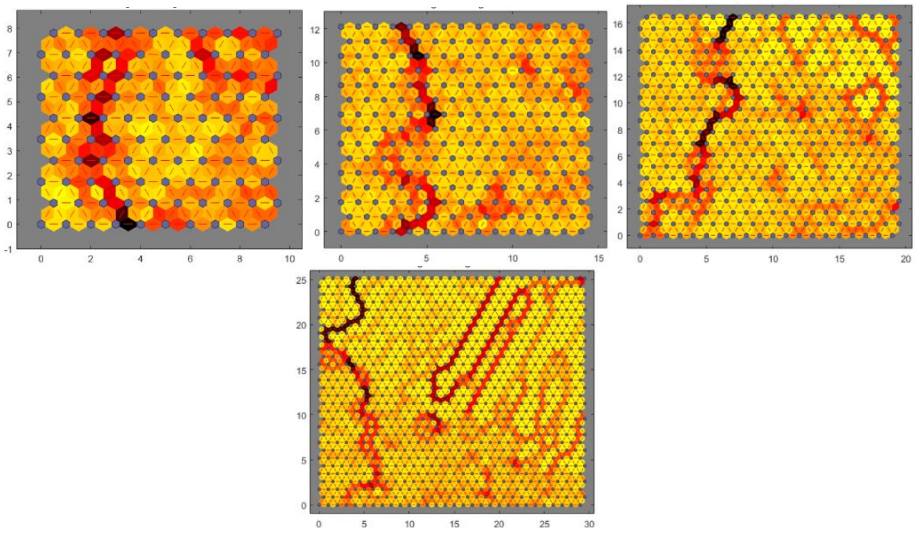

Fig. 10. The connections in different layers of SOM.

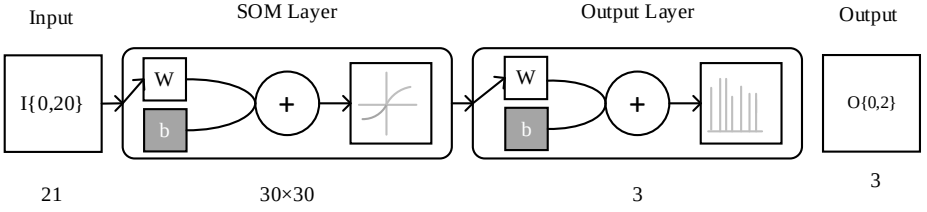

Fig.11. Output classification neural networks as part of the SOM layer.

4.3 Comparison Analysis

For different segmentation algorithms, the pixel accuracy, frequency-weight cross-combination ratio, over-segmentation rate and other indicators can used for comparative research. TABLE II shows the processing time consumed, mini-batch accuracy, mini-batch loss and learning rate of the proposed methos. TABLE III presents the performance of the algorithms of the proposed segmentation method by comparing to other deep learning methods.

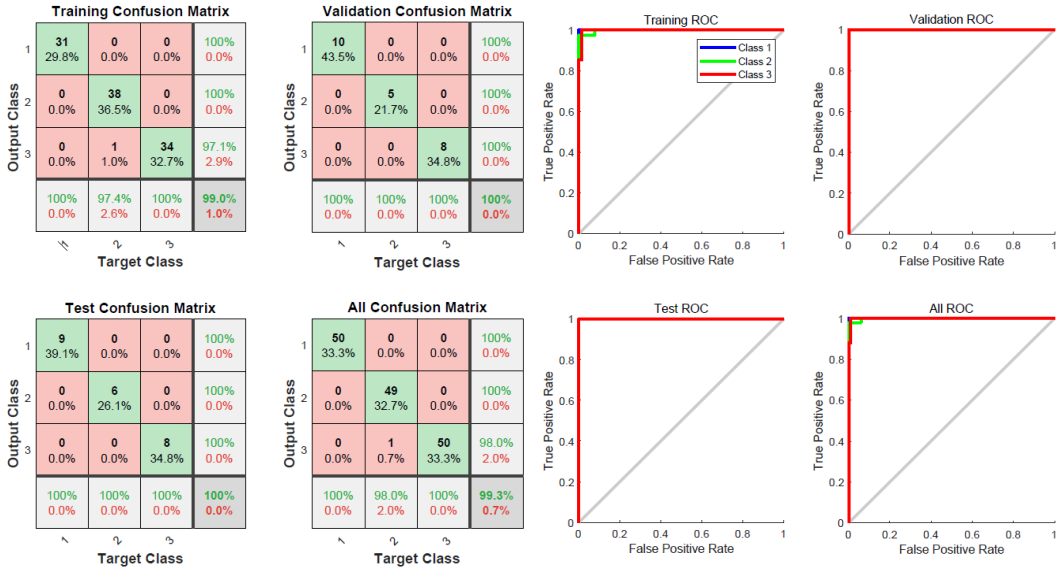

(a) (b)

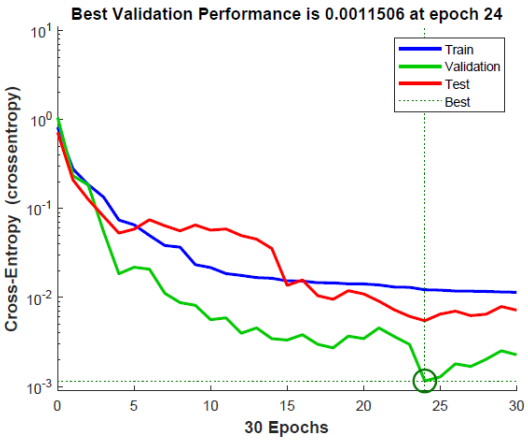

(c)

Fig. 12. An evaluation of the proposed neural networks for the classification of plantar pressure datasets; (a) classification confusion matrix, (b) training ROC, (c) the performance of the proposed network.

TABLE II Region-based Level Set Segmentation for Plantar Pressure Image Dataset

Iteration	Processing time	Multi-batch accuracy	Mini-batch loss	Learning rate
1	00:00:05	42.12%	0.4536	0.0010
10	00:00:42	47.34%	0.4844	0.0010
15	00:01:12	54.55%	0.5677	0.0010
20	00:01:45	73.23%	0.6899	0.0010

TABLE III Evaluation Indicators and Effects of Plantar Pressure Imaging Segmentation on Various Network Platforms

Methods	PA	MPA	MIoU	FWIoU	F1
Distance regularization level set (Zou et al. 2022)	0.701	0.721	0.625	0.795	0.475
Single seed region Growth Segmentation (Marosán et al. 2021)	0.712	0.725	0.709	0.725	0.582
Single segNet segmentation (Mythili et al. 2022)	0.783	0.772	0.685	0.785	0.523
LS-SOM neural network (proposed work)	0.811	0.802	0.611	0.786	0.620

PA-Pixel Precision; MPA- Mean Pixel Accuracy; MIoU-Mean Intersection over Union; FWIoU- Frequency Weight Intersection over Union

5 Conclusions

Segmentation of the plantar pressure image is crucial to feature extraction and key interest region extraction from the plantar pressure image set. A support point set will be formed for the optimized shoe-last surface based on the extraction of these critical regions. Using segmentation research on plantar pressure image set region growth, this study investigates the effectiveness of region-based level set segmentation. Data processing and analysis combined with the characteristics of artificial intelligence have gradually created a unique scientific system with the development of artificial intelligence and computer application technology, and new processing technologies, methods, and research directions have emerged as a result. Not only is traditional image processing technology complex, but it also has large application limitations and poor stability. Feature calculation and extraction algorithms are also subject to the weakness of combining diversity with classifiers. With the development of deep learning technology and deep neural networks, image segmentation has become more refined.

This study proposes a novel method for customizing shoe lasts using LS-SOM neural networks and domain-based segmentation models. This can lead to more accurate and personalized shoe design, improving wearer comfort and foot health. The optimization of shoe last design based on plantar pressure imaging data may improve wearing comfort and alleviate foot related issues, especially for people with hypertension and other diseases. This may help improve foot health outcomes and overall quality of life. For future work, foot pressure imaging data collection may be challenging and may require specialized equipment and protocols. The limited availability of high-quality data may hinder the universality and scalability of the proposed method. Although this study validated the proposed method using quantitative indicators,

further validation may be needed in real-world environments such as clinical trials or user studies to evaluate its effectiveness in practical applications. This may involve evaluating the impact of customized shoe lasts on wearer comfort, gait dynamics, and foot health outcomes.

Acknowledgement

This work is supported by Zhejiang Province Higher Education Visiting Engineer School-Enterprise Cooperation Project: Research and Application of Comfortable Shoes Based on Plantar Pressure Imaging Technology under grant no. FG2022054, and Wenzhou Polytechnic College Industry-Education Integration Project: Construction of Footwear Studio for Chain Integration of "Enterprise-School-Locality" under grant no. WZYCJRH202205.

References

J C. R. Pereira, M. B. Criado, J. Machado, C. T. Pereira, and M. J. Santos 2021. Acute effects of acupuncture in balance and gait of Parkinson disease patients – a preliminary study. Complementary Therapies in Clinical Practice. 45: 101479.

Z. Gao, C. Li, H. Hu, H. Zhao, C. Chen, and H. Yu 2016. Simulator study of young driver's instinctive response of lower extremity to a collision. Traffic Injury Prevention. 17(4): 423-429.

X. Li, Y. Jiang, M. Li, and S. Yin 2021. Lightweight attention convolutional neural network for retinal vessel image segmentation. IEEE Trans. Ind. Informat. 17(3): 1958-1967.

G. J. Aguiar, R. G. Mantovani, S. M. Mastelini, A. C. P. F. L. de Carvalho, G. F. C. Campos, and S. B. Junior 2019. A meta-learning approach for selecting image segmentation algorithm. Pattern Recognition Letters. 128: 480-487.

Y. Liu, C. He, P. Gao, Y. Wu, and Z. Ren 2019. A binary level set variational model with L1 data term for image segmentation. Signal Processing. 155:193-201.

Patel RK, Kashyap M. 2023. Automated screening of glaucoma stages from retinal fundus images using BPS and LBP-based GLCM features. International Journal of Imaging Systems and Technology. 33(1):246-61.

C. DiMattina 2022. Luminance texture boundaries and luminance step boundaries are segmented using different mechanisms. Vision Research. 190:107968.

C. Wu, B. Yi, Y. Zhang, S. Huang, and Y. Feng 2018. Retinal vessel image segmentation based on improved convolutional neural network. Acta Optica Sinica. 38(11):133-139.

Chouhan, S.S., Kaul, A. & Singh, U.P. 2018. Soft computing approaches for image segmentation: a survey. Multimed Tools Appl. 77:28483-28537

C. Wang, D. Li, Z. Li, D. Wang, N. Dey, A. Biswas, L. Moraru, R.S. Sherratt, and F. Shi 2019. An efficient local binary pattern based plantar pressure optical sensor image classification using convolutional neural networks. Optik. 185:543-557.

R. Kemker, C. Salvaggio, and C. Kanan 2018. Algorithms for semantic segmentation of multispectral remote sensing imagery using deep learning. ISPRS J. Photogrammetry and Remote Sensing. 145(part A):60-77.

H. Hofbauer, E. Jalilian, and A. Uhl 2019. Exploiting superior CNN-based iris segmentation for better recognition accuracy. Pattern Recognition Letters. 120:17-23.

P. Zhang, W. Liu, H. Wang, Y. Lei, and H. Lu 2019. Deep gated attention networks for large-scale street-level scene segmentation. Pattern Recognition. 88:702-714.

A. Dhomne, R. Kumar, and V. Bhan 2018. Gender recognition through face using deep learning. Procedia Computer Science.132: 2-10.

T. R. Chavan and A. V. Nandedkar 2018. AgroAVNET for crops and weeds classification: A step forward in automatic farming. Computers and Electronics in Agriculture. 154: 361-372.

B. Sateesh Babu, S. Suresh, K. Uma Sangumathi, and H. J. Kim 2012. A projection-based learning meta-cognitive RBF network classifier for effective diagnosis of Parkinson's disease. in: J. Wang, G. G. Yen, and M. M. Polycarpou (eds), Advances in neural networks, Lecture Notes in Computer Science. 7368, pp.611-620. Springer.

O. Erkaymaz, M. Özer, and N. Yumuşak 2012. Performance analysis of a feed-forward artificial neural network with small-world topology. Procedia Technology. 1: 291-296.

S. Dharini and J. Sanjay 2021. An efficient and hybrid pulse coupled neural network - based object detection framework based on machine learning. Computers & Electrical Engineering. 96(part B):107615.

T. Kohonen 2021. An Overview of SOM Literature, in: "Self-organizing maps," Springer Series in Information Sciences, 30.pp.277-301

M. N. Y. Ali, M. G. Sarowar, M. L. Rahman, J. Chaki, N. Dey, and J. M. R. S. Tavares 2019. Adam deep learning with SOM for human sentiment classification. Int. J. Ambient Computing and Intelligence. 10(3): 92-116.

M. S. Kamal, M. G. Sarowar, N. Dey, A. S. Ashour, S. H. Ripon, B. K. Panigrahi, and J. M. R. S. Tavares 2017. Self-organizing mapping-based swarm intelligence for secondary and tertiary proteins classification. Int. J. Machine Learning and Cybernetics.10(2):229-252.

L.-C. Chang, H.-Y. Shen, and F.-J. Chang 2014. Regional flood inundation nowcast using hybrid SOM and dynamic neural networks. J. Hydrology. 519(part A): 476-489.

Patel RK, Kashyap M. 2023. The study of various registration methods based on maximal stable extremal region and machine learning. Computer Methods in Biomechanics and Biomedical Engineering: Imaging & Visualization. 11(6):1-8.

Kimmel, R. 2004. The Osher-Sethian Level Set Method. In: Numerical Geometry of Images. Springer, New York, NY, 2004.

S. Li and P. Li 2018. Image segmentation and selective smoothing based on p-harmonic Mumford-Shah functional. Optik. 168:13-26.
S. Aly and S. Almotairi 2020. Deep convolutional self-organizing map network for robust handwritten digit recognition. IEEE Access. 8:107035-107045.
Z. Li, D. Wang, N. Dey, A. S. Ashour, R. S. Sherratt, and F. Shi 2019. Plantar pressure image fusion for comfort fusion in diabetes mellitus using an improved fuzzy hidden Markov model. Biocybernetics and Biomedical Engineering. 39(3):742-752.
M. A. Al-masni, M. A. Al-antari, M. T. Choi, S.-M. Han, and T.-S. Kim 2018. Skin lesion segmentation in dermoscopy images via deep full resolution convolutional networks. Computer Methods and Programs in Biomedicine. 162:221-231.
L. Zou, T. Weise, Q.-J. Huan, Z.-Z. Wu, L.-T. Song, and X.-F. Wang 2022. Distance regularization energy terms in level set image segment model: A survey. Neurocomputing. 491:244-260.
P. Marosán, K. Szalai, D. Csabai, G. Csány, A. Horváth, and M Gyöngy 2021. Automated seeding for ultrasound skin lesion segmentation. Ultrasonics. 110:106268.
T. Mythili and A. Anbarasi 2022. A concatenation of deep and texture features for medicinal trash image classification using EnSeg-Net-DNN-based transfer learning. Materials Today: Proceedings. 62(part 7):4691-4698.